Journal of The
Electrochemical Society

You may also like

- Synergetic Effects between a Bipyridyl-Functionalized Metal-Organic Framework and Graphene for Sensitive Electrochemical Detection of Norepinephrine
Lu-Lu Gao, Jia-Jia Fang, Ning-Ning Yang et al.

- Engineering Low Cost ZnO/RGO Nanocomposite for the Picomolar Sensing of Epinephrine, Uric Acid and Tyrosine
Teena Joseph, Jasmine Thomas, Tony Thomas et al.

- A Surface Network Based on Reduced Graphene Oxide/Gold Nanoparticles for Selective Determination of Norepinephrine in Real Samples
Emad A. Khudaish and Ameera Al-Khodouri

$Ti_3C_2T_x$ MXene/CeO_2-Integrated Graphite Conductive Ink Based Flexible Electrode for Norepinephrine Detection

To cite this article: Selen Uruc *et al* 2026 *J. Electrochem. Soc.* **173** 167502

View the article online for updates and enhancements.

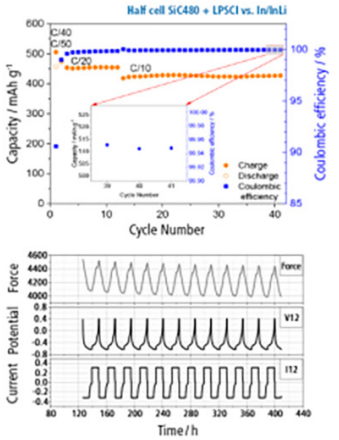
The New PAT-Cell-Solid!

EL-CELL®
electrochemical test equipment

Cycle Solid-State Batteries Under Controlled Pressure of up to 300 MPa (6 mm Diameter)!



- Adjust and measure a force of up to 9000 N on the cell stack!
  Force adjustment possible throughout the entire experiment
- Built-in force, and temperature sensors!
  With optional gas pressure sensor and gas in- and outlet
- PAT-Solid-Core for easy assembly and reproducible results!
  Press and cycle solid-state batteries with 6 or 10 mm electrode diameter
- Cableless and highly sealed battery test cell!
  For precise long-term measurements of solid-state cell chemistries



Learn more on our product website:
Scan me!

Download the data sheet (PDF):
Scan me!

Or contact us directly:
+49 40 79012-734
sales@el-cell.com
www.el-cell.com

This content was downloaded from IP address 193.140.1.200 on 07/09/2026 at 22:09

Journal of The Electrochemical Society, 2026 **173** 167502
1945-7111/2026/173(16)/167502/13/$40.00 © 2026 The Electrochemical Society ("ECS"). Published on behalf of ECS by IOP Publishing Limited. All rights, including for text and data mining, AI training, and similar technologies, are reserved.

$Ti_3C_2T_x$ MXene/CeO_2-Integrated Graphite Conductive Ink Based Flexible Electrode for Norepinephrine Detection

Selen Uruc, Ozge Gorduk, Semih Gorduk, and Yucel Sahin[z]

Department of Chemistry, Faculty of Arts and Science, Yildiz Technical University, Istanbul, TR34220, Turkey

The development of conductive and sustainable materials with high electrochemical performance remains an important goal for next-generation sensing platforms. In this study, a flexible electrochemical sensor was fabricated on a low-cost cellulose-based paper substrate using an MXene/cerium oxide/graphite (MXene/CeO_2/G) composite conductive ink. The conductive ink was formulated by dispersing MXene, CeO_2, and graphite as individual components within the same matrix, forming a composite structure. This combination improved both the electrical conductivity and the electrocatalytic activity toward norepinephrine (NE) oxidation. The electrochemical behavior of the MXene/CeO_2/G screen-printed electrode (SPE) was investigated, and the oxidation process was found to be diffusion and adsorption-controlled. The electroactive surface area of the electrodes was also determined, indicating an increased number of active sites. The effect of pH was examined, and the highest current response was obtained at pH 6.4. Under optimized conditions, the sensor exhibited a detection limit (LOD) of 77.29 nM and a linear range of 0.25–25 μM using differential pulse voltammetry (DPV). The sensor showed good selectivity in the presence of common interfering species. Recovery values ranged between 95.1% and 107.0%, with low relative standard deviation (RSD), confirming the reliability of the method. The applicability of the sensor was demonstrated in artificial urine samples. These results demonstrate that MXene/CeO_2/G-based conductive inks provide a promising approach for the development of flexible and cost-effective electrochemical sensors.
© 2026 The Electrochemical Society ("ECS"). Published on behalf of ECS by IOP Publishing Limited. All rights, including for text and data mining, AI training, and similar technologies, are reserved. [DOI: 10.1149/1945-7111/ae9649]

Manuscript submitted June 6, 2026; revised manuscript received July 26, 2026. Published August 19, 2026.

Supplementary material for this article is available online

Norepinephrine (NE, noradrenaline, $C_8H_{11}NO_3$) is one of the primary catecholamines in the human body and functions both as an important neurotransmitter and as a hormone secreted by the adrenal medulla.[1] It plays a central role in regulating wakefulness, attention, and stress responses, while also acting as a major mediator of sympathetic nervous system activity.[2] In healthy adults, basal plasma levels of NE typically range from 0–60 pg ml^{-1}, while total urinary excretion is around 15–80 ng ml^{-1}.[3] Imbalances in NE levels are associated with a wide variety of pathological conditions. Specifically, elevated NE levels are linked to stress, hypertension, thyroid hormone deficiency, arrhythmias, and congestive heart failure, whereas low levels are associated with hypotension as well as neurological disorders such as depression, Alzheimer's disease, and Parkinson's disease. Additionally, it has been demonstrated that NE plays a role in systemic conditions such as diabetes, DNA damage, and HIV-1-related pathologies.[4,5] Beyond its neurological functions, NE's involvement in broader metabolic and cellular damage processes makes it a clinically significant biomarker.

In view of these significant clinical implications, the detection of NE in biological fluids, including blood plasma, urine, and cerebrospinal fluid (CSF), is of great diagnostic importance. Furthermore, the determination of NE in alternative biological matrices such as urine, saliva, and sweat has emerged as a promising area for non-invasive health monitoring approaches and has enabled real-time physiological assessment.[6] A variety of analytical techniques have been developed for the precise and reliable quantification of NE in such complex matrices, owing to their high sensitivity and selectivity. These techniques include spectrophotometry, high-performance liquid chromatography, ion chromatography, and fluorimetry.[7–10] However, these methods generally face significant challenges, including high costs, lengthy sample pretreatment protocols, and the need for extensive laboratory infrastructure.[5] These limitations have driven the development of alternative strategies based on electrochemical reactions of NE molecules. In this context, non-enzymatic electrochemical methods supported by robust nanomaterials have emerged as a strong alternative. These methods offer superior environmental stability, cost-effectiveness, ease of use, high sensitivity, and selectivity.

Conductive inks play a key role in the development of flexible and wearable electrochemical sensors. These inks consist of three main components that collectively determine their electrical and mechanical properties.[11] The first component is the conductive material, which provides electrical conductivity. The second is the binder, which holds the conductive particles together, promotes their adhesion to the substrate, and supports the formation of a continuous conductive network. The third component is the solvent, which maintains the other constituents in suspension and imparts the viscosity required for the selected printing technique.[12]

Conductive materials play a critical role in conductive ink formulations by providing electrical conductivity, which is the primary function of the ink. They are also among the key components that directly influence the performance, cost, and practical applicability of the resulting sensor. Their principal function is to form a continuous conductive network after the ink has dried and the binder matrix has solidified.[13] The most commonly used conductive materials include metallic nanoparticles and carbon-based materials such as graphite, graphene, and carbon nanotubes. Among these, metal-and carbon-based conductive inks are widely employed in the fabrication of electrochemical sensors. In addition, composite inks containing different classes of conductive and electroactive materials have attracted considerable attention because they can combine the complementary electrical, electrochemical, and structural properties of their individual constituents.

Among the conductive and electroactive nanostructured materials incorporated into such composite ink formulations, MXenes and cerium oxide (CeO_2) nanoparticles have attracted considerable attention owing to their favorable electrical and catalytic properties. MXenes are a family of two-dimensional transition-metal carbides and nitrides with the general formula $M_{n+1}X_nT_x$. $Ti_3C_2T_x$, one of the most widely investigated MXenes, exhibits high electrical conductivity, a large specific surface area, tunable surface chemistry, and mechanical flexibility. These properties promote efficient charge transport and strengthen the interactions between the electrode surface and target analytes, thereby facilitating rapid electron transfer.[14,15] On the other hand, CeO_2 nanoparticles, which act as an electroactive and catalytic component in conductive ink formulations, are also widely used in electrochemical applications owing to their high ionic conductivity, large surface area, and stable fluorite crystal structure.[16] The reversible Ce^{4+}/Ce^{3+} redox

[z] E-mail: yucelsahin06@gmail.com

couple promotes oxygen mobility and enhances surface reactivity, resulting in improved catalytic activity and electrochemical performance.[17] Therefore, the combined incorporation of $Ti_3C_2T_x$ MXene and CeO_2 nanoparticles into a graphite-based conductive matrix represents a promising synergistic strategy for the development of high-performance electrochemical sensing interfaces. In this composite system, MXene provides efficient electron-transport pathways and a highly accessible electroactive surface, whereas CeO_2 contributes redox activity and catalytic functionality. Their simultaneous incorporation into the conductive ink can therefore improve both the electrical properties of the printed electrode and its electrochemical response toward the target analyte.

While the selection and combination of conductive and electroactive materials are essential for achieving high electrochemical performance, the structural configuration of the sensing platform is equally important for the development of practical diagnostic systems. In this respect, flexible and wearable electrochemical sensors have emerged as prominent platforms among next-generation sensing technologies.[18] The development of analyte-specific conductive inks represents an effective strategy for integrating both electrical conductivity and sensing functionality directly into electrode structure.[19] Unlike conventional rigid electrodes that often require additional surface-modification steps, functional conductive inks enable active nanomaterials to be incorporated directly into printable formulations and deposited onto a variety of flexible substrates.[20] This fabrication approach supports the development of lightweight, portable, and user-friendly point-of-care (POC) systems and may facilitate real-time and continuous monitoring of physiologically relevant analytes. Among the available flexible substrates, paper-based materials have attracted considerable attention because of their low cost, ease of processing, mechanical flexibility, sustainability, and biodegradability.

In this study, a flexible electrochemical sensing platform based on a specially designed MXene/CeO_2/graphite-based conductive ink is presented. The prepared ink was then employed to fabricate electrodes via screen printing onto a flexible paper-based substrate, thereby establishing a low-cost and scalable production strategy. The utilization of the aforementioned MXene/CeO_2/G/SPE facilitated the determination of NE via differential pulse voltammetry (DPV), achieving a linear range of 0.25–25 μM and a LOD of 77.29 nM, along with satisfactory recovery and high reproducibility. This enhanced performance can be attributed to the high electrical conductivity and large surface area of MXene, which facilitate rapid electron transfer and increase active reaction sites. These properties are further enhanced by the Ce^{4+}/Ce^{3+} redox cycle in the CeO_2 structure, which contributes to high catalytic activity for the oxidation of NE. These results demonstrate that the proposed platform holds significant promise for next-generation flexible electrochemical sensing applications.

Experimental

Chemicals and apparatus.—Full details of the chemicals, reagents, and instrumentation used throughout this study are available in the Supplementary Material document.

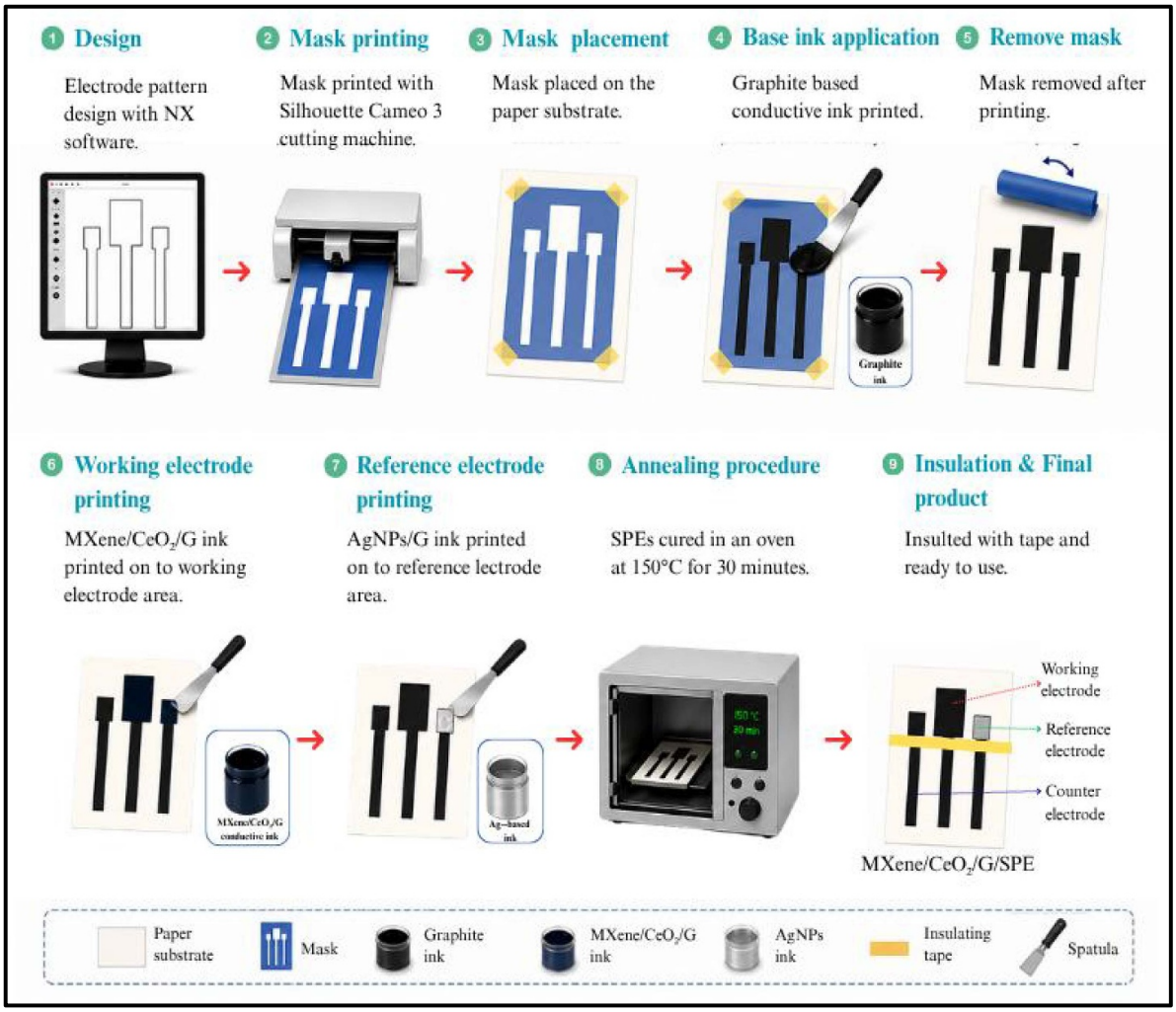
Synthesis of $Ti_3C_2T_x$ MXene.—$Ti_3C_2T_x$ MXene was synthesized via selective etching of the Ti_3AlC_2 MAX phase using a previously reported method with minor modifications.[21] Briefly, 100 ml of 1% HF solution was transferred into a Teflon container, and Ti_3AlC_2 powder was gradually added under continuous stirring. The etching process was carried out at approximately 25 °C for 3 h. Subsequently, 300 ml of ultrapure water was added, and the mixture was centrifuged at 4000 rpm for 15 min. The sediment was collected and washed repeatedly with ultrapure water until a neutral pH was achieved. The product was then dried at 100 °C for 6 h. A portion of the dried powder (2.5 g) was redispersed in 400 ml of ultrapure water and ultrasonicated for 2 h to achieve exfoliation. After centrifugation, a stable black colloidal suspension was obtained, filtered, and dried at 100 °C for 24 h. Delamination of MXene was carried out in deionized water in the absence of supplementary delaminating agents, and the obtained material was subsequently dried under vacuum at 35 °C for 24 h. All HF handling procedures were performed under appropriate safety precautions.

Synthesis of cerium oxide (CeO_2) nanoparticles.—CeO_2 nanoparticles were synthesized via a precipitation method based on a previously reported procedure.[22] Briefly, 0.01 mol of $Ce(NO_3)_3{\cdot}6H_2O$ was dissolved in 50 ml of ultrapure water under continuous stirring. NH_4OH was then added dropwise until the pH reached 9, resulting in the formation of a cerium hydroxide precipitate. The precipitate was washed several times with ultrapure water and dried at 150 °C for 24 h. The dried product was subsequently calcined at 400 °C for 2 h to obtain crystalline CeO_2 nanoparticles.

Formulation of AgNPs-based conductive ink for reference electrode.—A conductive ink containing silver nanoparticles (AgNPs) was prepared for use as the pseudo-reference electrode (hereafter referred to as Ag conductive ink). AgNPs were synthesized according to a previously reported method using glucose as the reducing agent and PVP as the stabilizer. Briefly, $AgNO_3$ solution was gradually added to a 30 ml alkaline solution containing 5.4 g glucose and 0.3 g PVP and stirred at 70 °C for 1 h. The obtained AgNPs were filtered and dried. Then, the AgNPs-based conductive ink was prepared. To do this, 100 mg of carboxymethyl cellulose (CMC) was dissolved in 1.0 ml of distilled water at room temperature under continuous stirring. Subsequently, 150 mg of AgNPs were added and the mixture was thoroughly homogenized until a uniform conductive ink was obtained.[23]

Preparation of MXene/CeO_2/G conductive ink.—Two different conductive inks were prepared for the fabrication of flexible electrodes for NE detection. The first ink was used as a ground (base) ink, while the second was a functional conductive ink containing electrocatalytic materials for the working electrode. The graphite-based ink consisted of 1.5 ml of water, 1.5 ml of ethanol, 100 mg of CMC as a binder, and 400 mg of G. For the working electrode, an MXene/CeO_2/G-based conductive ink was prepared. To optimize the ink composition, a series of experiments were conducted. Briefly, 100 mg of CMC was dissolved in a solvent system containing 2.0 ml of water and 1.0 ml of ethanol under continuous stirring. Subsequently, 400 mg of G, 10 mg of MXene, and 75 mg of CeO_2 nanoparticles were added. The mixture was stirred at room temperature (Scheme 1). After mechanical stirring, homogeneous conductive ink was obtained without any visible agglomeration or phase separation. The resulting suspension exhibited a slightly viscous consistency, which was suitable for reproducible electrode modification and printing processes. The resulting ink was directly suitable for the printing process without further treatment.

Production of MXene/CeO_2/G/SPE.—Stencils used for the fabrication of SPEs were designed utilizing Siemens NX software and fabricated with a Silhouette Cameo 4 cutting machine. The geometric surface areas of the working, counter, and reference electrodes were 28, 13.5, and 13.5 mm^2, respectively. The stencils were placed on paper substrates, and a graphite-based conductive ink was applied using a spatula, followed by careful removal of the stencils. For the working electrode, an MXene/CeO_2/graphite conductive ink was printed onto the substrate using a mask to ensure precise deposition. Subsequently, an AgNP-based conductive ink was applied to form the reference electrode. The fabricated SPEs were annealed at 150 °C for 30 min, insulated with tape, and prepared for electrochemical measurements. A schematic illustration of the flexible electrode fabrication process is shown in Scheme 1. Furthermore, Fig. S1 includes



Scheme 1. Schematic representation of the preparation of MXene/CeO_2/G printed flexible electrode.

a photograph of the twisted MXene/CeO_2/G/SPE, visually demonstrating the flexibility of the electrode and the strong adhesion of the conductive ink to the substrate.

Non-enzymatic detection of NE at MXene/CeO_2/G/SPE.—Electrochemical measurements were carried out in 0.1 M phosphate-buffered saline (PBS, pH 6.4) containing 25 μM NE and 0.1 M KCl using cyclic voltammetry (CV) and differential pulse voltammetry (DPV). CV measurements were conducted at a scan rate of 100 mV s^{-1} over a potential range from −0.4 V to + 0.65 V, while DPV measurements were performed within the potential window of −0.2 V to + 0.6 V.

Preparation of the artificial urine sample.—To evaluate the applicability of the MXene/CeO_2/G/SPE for NE detection, an artificial urine matrix was employed. The artificial urine solution was prepared by dissolving creatinine, KH_2PO_4, NaCl, $CaCl_2 \cdot 2\ H_2O$, urea, Na_2SO_4, KCl, and NH_4Cl in deionized water. Before electrochemical measurements, the prepared artificial urine was diluted ten-fold to obtain the working sample.[24]

Results and Discussion

Optimization of conductive ink composition and electrode annealing processes.—The electrochemical performance of the MXene/CeO_2/G/SPE for NE determination is strongly governed by the conductive ink composition and fabrication parameters. Therefore, key parameters, including solvent composition, G loading, binder content, MXene and CeO_2 ratios, as well as annealing conditions, were systematically optimized based on DPV responses. Throughout all optimization steps, a solution of 0.1 M PBS at pH 6.4 and 0.1 M KCl containing 25 μM NE was used.

The solvent system plays a critical role in determining ink processability and film formation. A binary solvent system consisting of water:ethanol was utilized, and electrode performance was evaluated at different solvent ratios (Fig. 1a). Among the tested compositions, the system containing 2.0 ml water and 0.5 ml ethanol exhibited the highest oxidation peak current of +1.86 μA at +0.19 .[25,26,27] This enhancement is attributed to improved wettability and the formation of a more homogeneous conductive network due to the reduced surface tension in the presence of ethanol. In contrast, higher ethanol content decreased the solubility of CMC, adversely affecting the integrity of the ink film.[28,29]

The solid loading was optimized to achieve an appropriate balance between viscosity and electrochemical performance of the conductive ink. In this context, the total solid content was tuned by varying the G loading (200–600 mg) while keeping the MXene, CeO_2, and binder content constant. As can be seen in Fig. 1b, increasing the G loading significantly influenced the formation of conductive pathways, with the oxidation peak current increasing markedly up to 400 mg due to the formation of an effective percolation network.[30,31] At higher G loadings, however, a decline in performance was observed, likely due to the dilution of electrochemically active

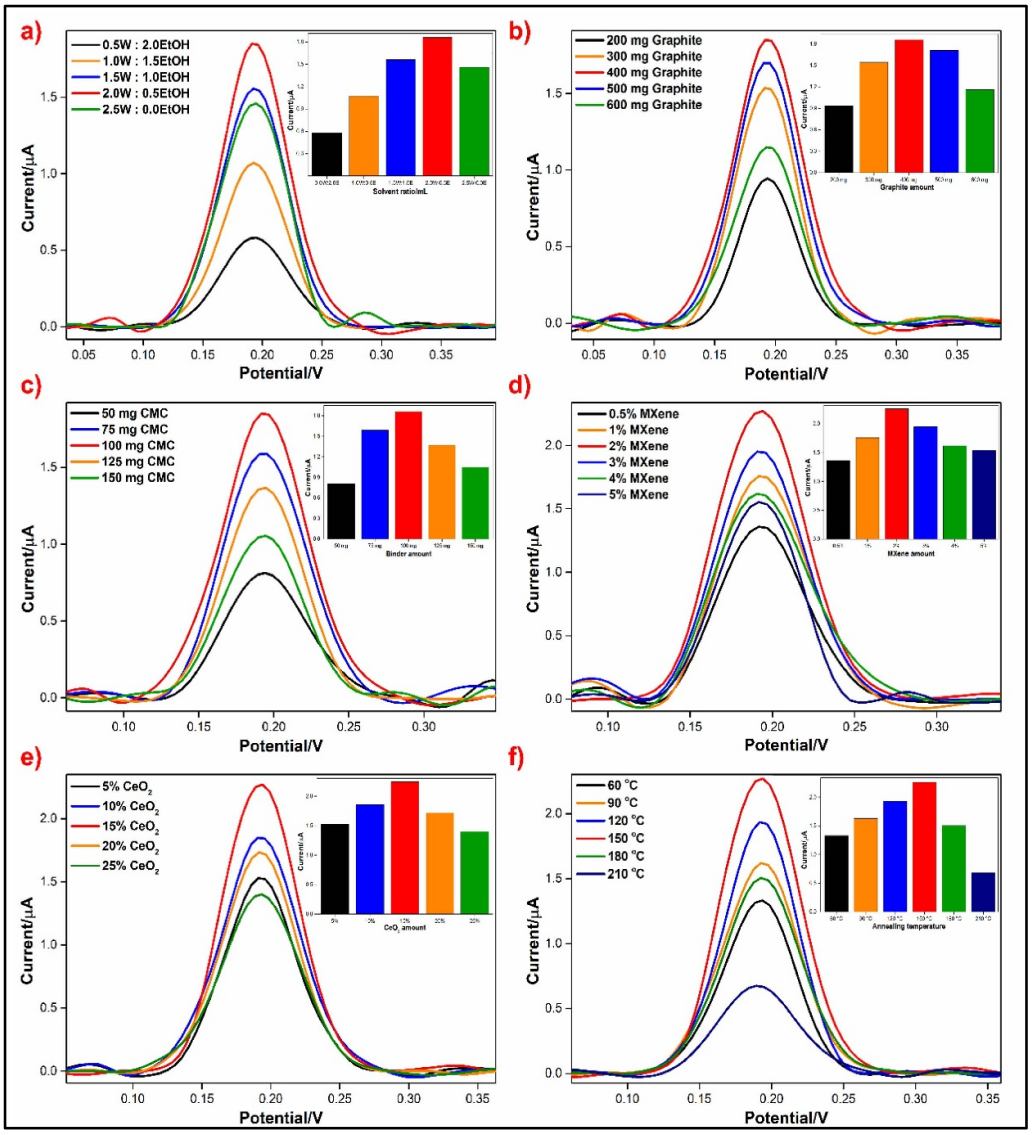


Figure 1. Optimization of MXene/CeO_2/G conductive ink components and annealing parameters in 0.1 M pH 6.4 PBS and 0.1 M KCl solution containing 25 μM NE: (a) solvent ratio, (b) G, (c) CMC, (d) MXene, (e) CeO_2 amount, and (f) annealing temperature.

components and a reduction in the effective electroactive surface area.[32]

The binder content is another critical parameter in the optimization of the conductive ink formulation. In this study, CMC was selected as the binder due to its strong adhesion properties arising from its high hydroxyl group content. The electrochemical performance of electrodes prepared with varying CMC amounts is shown in Fig. 1c. The highest oxidation peak current was obtained with 100 mg of CMC. This behavior is attributed to improved interparticle adhesion and enhanced continuity of the conductive network.[28] However, further increases in CMC content led to a decline in performance due to the formation of insulating regions, which hindered electron transfer.[31,33]

The effect of the MXene amount was also examined in detail. As demonstrated in Fig. 1d, an augmentation of the MXene content to 2% resulted in a substantial enhancement of the oxidation peak current. This phenomenon can be ascribed to the high electrical conductivity and substantial specific surface area inherent to MXene. These properties serve to increase the density of electroactive regions, thereby supporting efficient interaction between norepinephrine molecules and the electrode surface.[34] However, further increases in the amount of MXene resulted in a gradual decrease in the current response. This phenomenon is primarily attributed to the re-stacking and aggregation of the nanosheets, which limit the accessible surface area and hinder electron transfer.[35]

Similarly, the effect of CeO_2 amount was evaluated within the 5%–25% (w/w) range (Fig. 1e). The oxidation peak current exhibited a consistent increase as the CeO_2 content rose to 15%, which can be attributed to the catalytic contribution provided by the reversible Ce^{4+}/Ce^{3+} redox pair and its role in augmenting the electroactive surface area.[36] Furthermore, moderate CeO_2 loading enhanced the interfacial contact between the conductive components.[37] However, loadings beyond this threshold resulted in diminished performance; this can be ascribed to the agglomeration of nanoparticles and the formation of partially insulating regions, thereby disrupting the conductive pathways.[38] Moreover, an excess of CeO_2 content was found to reduce the composite's overall electrical conductivity due to its comparatively lower intrinsic conductivity compared to the MXene and graphite framework.[39]

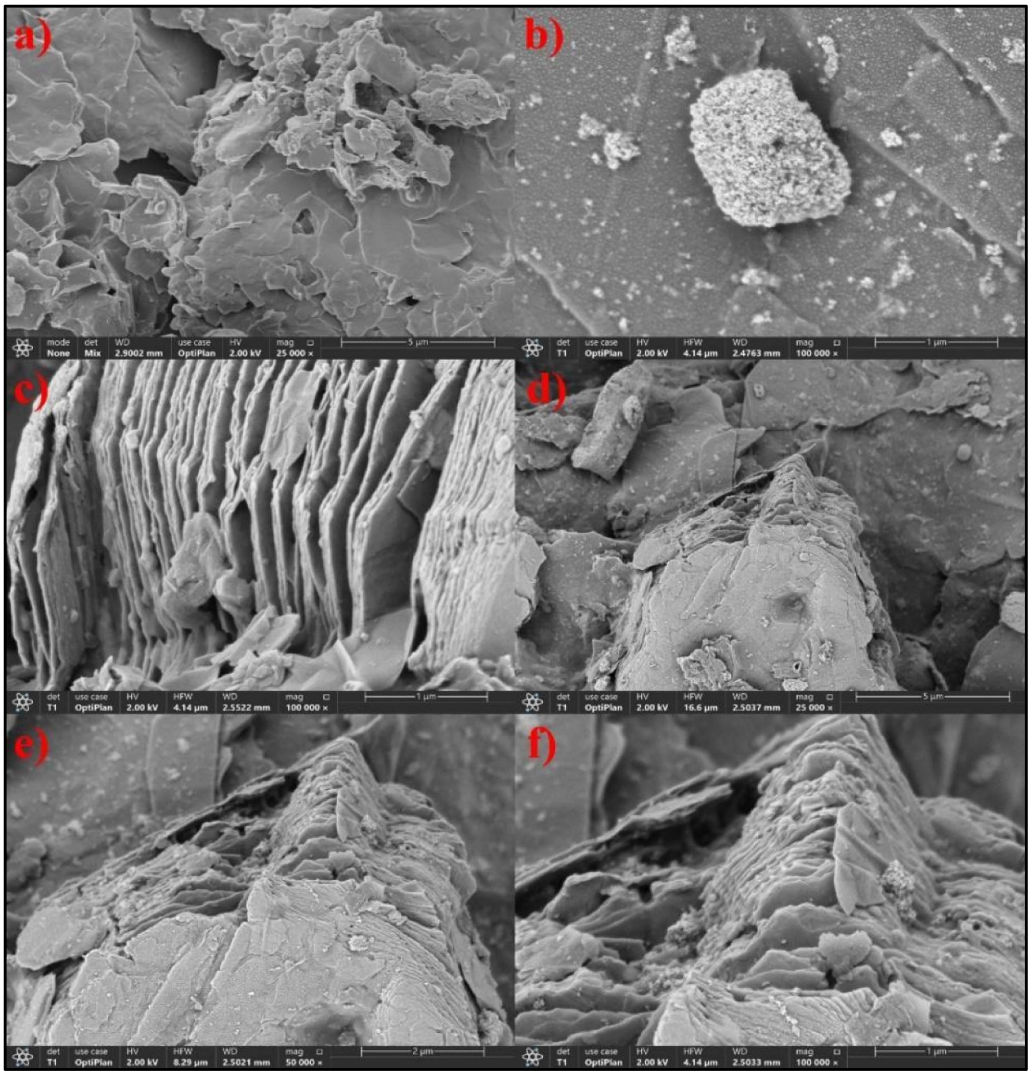


Figure 2. FESEM micrographs of (a) G/SPE at 25 000×, (b) CeO_2/G/SPE at 100 000×, (c) MXene/G/SPE at 100 000×, and MXene/CeO_2/G/SPE at (d) 25 000×, (e) 50 000×, and (f) 100 000× magnification.

The annealing process, which determines particle agglomeration and the formation of a conductive network, was systematically optimized in terms of both temperature and time. An increase in the annealing temperature from 60 °C to 150 °C resulted in a significant increase in peak current (Fig. 1f). This phenomenon can be attributed to two factors: increased interparticle contact and improved electrical conductivity.[40] However, further temperature increases resulted in a decline in performance, likely due to thermal degradation of the cardboard substrate and loss of mechanical integrity.[41] Consequently, 150 °C was identified as the optimal annealing temperature.

The annealing time showed a similar trend, and as shown in Fig. S2, the optimal time was determined to be 30 min. Insufficient annealing time prevents a complete conductive network, but longer times cause performance to drop. This is attributed to thermal degradation of the substrate and a possible reduction in the accessible active surface area.

In general, the optimized conditions (2.0 ml water:0.5 ml ethanol, 400 mg graphite, 100 mg CMC, 2% MXene, 15% CeO_2, 150 °C annealing temperature, and a 30 min annealing time) provided the optimal balance between conductivity, catalytic activity, and structural stability, leading to the highest electrochemical performance for NE detection.

Characterization studies of MXene/CeO₂/G/SPE.—The morphological features and elemental compositions of the G/SPE, CeO_2/G/SPE, MXene/G/SPE, and MXene/CeO_2/G/SPE were investigated using field-emission scanning electron microscopy (FESEM) and energy-dispersive X-ray spectroscopy (EDX). The FESEM micrograph of G/SPE at 25 000× magnification (Fig. 2a) displays well-defined layered G sheets uniformly distributed across the electrode surface, typical of graphitic carbon structures.[41] High-magnification images (100 000×) of CeO_2/G/SPE (Fig. 2b) and MXene/G/SPE (Fig. 2c) further elucidate the structural details. In Fig. 2b, spherical CeO_2 nanoparticles are observed both as fine clusters and uniformly dispersed particles on the graphite support.[42] Fig. 2c exhibits the characteristic two-dimensional, exfoliated nanosheet morphology of MXene, confirming successful delamination of the MAX phase.[43] Notably, the FESEM images of MXene/CeO_2/G/SPE at different magnifications (Figs. 2d–2f) reveal that CeO_2 nanoparticles are effectively anchored onto and partially intercalated between the MXene layers. This synergistic architecture prevents the restacking of MXene sheets, thereby maintaining a high electroactive surface area. Ultimately, the FESEM analysis confirms the successful integration of all components into a well-dispersed composite structure.

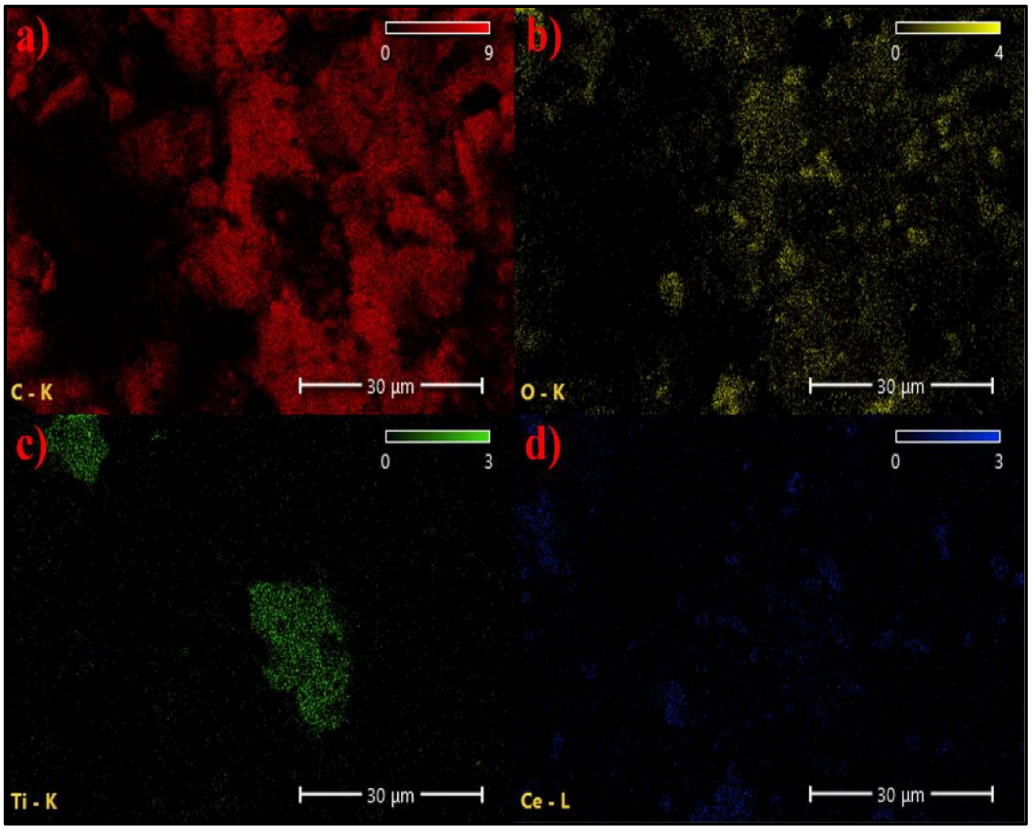


Figure 3. Elemental mapping of the MXene/CeO_2/G/SPE, showing the distribution and composition of (a) C, (b) O, (c) Ti, and (d) Ce elements across the electrode surface.

Element mapping and EDX analysis (Fig. 3) confirm the presence of the expected elements in the MXene/CeO_2/G/SPE. Quantitative results indicate that carbon (C) is the most prevalent element (71.9%), followed by oxygen (O, 20.1%), titanium (Ti, 4.5%), and cerium (Ce, 3.5%). These results confirm the successful fabrication of a well-integrated composite electrode.

The electrochemical properties of the flexible MXene/CeO_2/G/SPE sensor were evaluated using CV and electrochemical impedance spectroscopy (EIS) in 5.0 mM $[Fe(CN)_6]^{3-/4-}$ and 0.1 M KCl. As shown in Fig. 4a, The MXene/CeO_2/G/SPE exhibited the highest redox response (Ipa = + 45.04 µA; Ipc = −41.88 µA), significantly outperforming G/SPE (+9.63 and −7.88 µA), CeO_2/G/SPE (+20.09 and −18.76 µA), and MXene/G/SPE (+17.65 and −15.99 µA). The enhanced current at the MXene/G/SPE is attributed to MXene's 2D layered structure and high metallic conductivity, which expands the electroactive surface area.[34] The further increase in CeO_2 modified electrodes stems from the potent electrocatalytic activity of the Ce^{4+}/Ce^{3+} redox couple, facilitating the probe's electron transfer kinetics.[44] Ultimately, the MXene/CeO_2/G/SPE hybrid demonstrates a powerful synergy, merging MXene's high surface area and conductivity with CeO_2's catalytic prowess to maximize active sites.[45] Notably, despite the superior peak currents, the MXene/CeO_2/G/SPE showed an increased peak-to-peak separation (ΔEp) in Table S1. This localized retardation in electron transfer kinetics is likely due to the strong adsorption of redox probes and the interference of MXene's surface functional groups.[46,47]

The interfacial charge transfer dynamics were further elucidated using EIS. The Nyquist plots displayed in Fig. 4b were obtained by means of fitting the data to the equivalent circuit model provided in Fig. 4b inset. According to the Nyquist plots, the MXene/CeO_2/G/SPE exhibited the smallest semicircle diameter, yielding the lowest charge-transfer resistance (Rct = 576.1 Ω) compared to G/SPE (Rct = 1760 Ω), MXene/G/SPE (Rct = 855.9 Ω), and CeO_2/G/SPE (Rct = 711.8 Ω). This significant reduction in Rct confirms that the synergistic integration of MXene's high conductivity with CeO_2's catalytic Ce^{4+}/Ce^{3+} redox cycling effectively lowers the energy barrier for electron transfer at the electrode/electrolyte interface.[45] These results corroborate the CV findings, demonstrating that the composite SPE markedly accelerates charge transport despite the localized kinetic complexities observed in ΔEp.

The crystalline phase and structural integrity of the MXene/CeO_2/G/SPE were examined by X-ray diffraction (XRD) analysis (Fig. 4c). The diffraction peaks observed at 2θ = 26.5° and 42.3° are indexed to the (002) and (100) planes of graphitic carbon, respectively.[48,49] Distinct diffraction peaks at 2θ = 8.87°, 18.61°, 44.46°, and 59.11° confirm the presence of MXene, while the peaks at 2θ = 28.57°, 33.07°, 47.36°, and 56.20° correspond to the cubic fluorite structure of CeO_2.[50,51] Notably, the preservation of the MXene (002) peak without significant shifting indicates that the two-dimensional lamellar structure was maintained without substantial expansion or contraction of the interlayer spacing. These results confirm the successful integration of all components into the hybrid structure.

The surface functional groups and chemical environments of the MXene/CeO_2/G/SPE were investigated via Fourier transform infrared spectroscopy (FTIR) (Fig. 4d). The broad absorption band centered at 3433 cm^{-1} is attributed to the O–H stretching vibrations of adsorbed water molecules and surface hydroxyl groups. The peaks identified at 2924 cm^{-1} and 1625 cm^{-1} correspond to C–H and C=O stretching vibrations, respectively.[41] In the fingerprint region, distinct bands at 633 cm^{-1} and 857 cm^{-1} are assigned to the characteristic Ti–O and Ce–O lattice vibrations, respectively, confirming the successful integration of MXene and CeO_2 phases.[52,53] Furthermore,

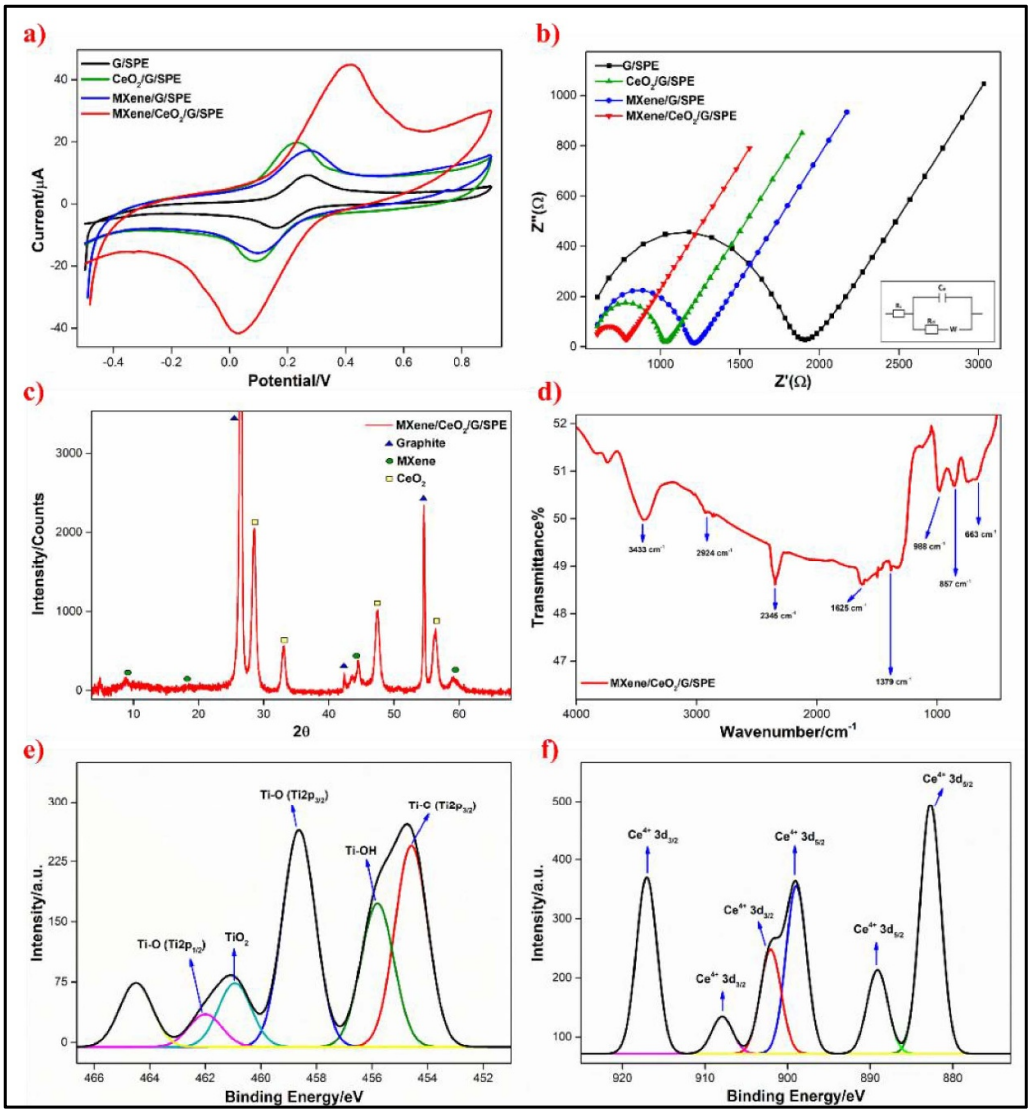


Figure 4. (a) Cyclic voltammograms and (b) Nyquist plots of prepared SPEs in 5.0 mM $[Fe(CN)_6]^{3-/4-}$and 0.1 M KCl solution, (c) XRD pattern, (d) FTIR spectrum, (e) Ti2p sub-binding, and (f) Ce3d sub-binding of MXene/CeO_2/G/SPE.

the peak at 988 cm^{-1} is associated with the C–F stretching from the MXene surface terminations (-F). These FTIR results, in conjunction with XRD data, provide definitive evidence for the successful chemical incorporation of MXene, CeO_2, and graphitic carbon within the hybrid SPE.

The surface elemental composition and chemical valence states of the MXene/CeO_2/G/SPE were investigated via X-ray photoelectron spectroscopy (XPS). The survey spectrum (Fig. S3) unequivocally confirms the presence of C1s (285.1 eV), O1s (532.8 eV), Ti2p (459.2 eV), and Ce3d (899.7 eV), validating the successful integration of all constituents. The high-resolution Ti2p spectrum (Fig. 4e) exhibits characteristic Ti–C doublets at 454.6 eV ($Ti2p_{3/2}$) and 462.0 eV ($Ti2p_{1/2}$), alongside peaks at higher binding energies associated with Ti–O and surface termination groups (-OH,-F). These features indicate partial surface oxidation, typical of delaminated MXene.[50,54] The Ce3d spectrum (Fig. 4f) displays a complex multiplet structure; the presence of "shake-up" satellites (notably at 916.7 eV) and peaks centered at 882.7 and 898.8 eV confirms that cerium predominantly exists in the Ce^{4+} oxidation state, consistent with the fluorite CeO_2 structure.[55] This multifaceted surface analysis provides definitive evidence for the successful formation of the hybrid architecture with preserved chemical integrity.

pH study.—The influence of pH on the oxidation mechanism of NE at the MXene/CeO_2/G/SPE was systematically investigated over a wide pH range (4.4–10.4). The differential pulse voltammograms (Fig. 5a) clearly demonstrate that increasing the pH leads to a gradual shift of the oxidation peak potential (Ep) toward less positive values. This negative shift reflects the involvement of protons in the oxidation process, indicating a proton–coupled electron transfer mechanism.[56] In addition to the potential shift, the peak current responses were also found to be pH dependent. The highest oxidation peak current was obtained at pH 6.4, with a value of + 2.82 μA at + 0.24 V, suggesting that this condition provides the most favorable electrochemical environment for NE detection.

The linear dependence of Ep on pH (Fig. 5b) further supports this interpretation. A well-defined linearity was observed across the studied pH range, with a slope of 56 mV pH^{-1}. According to the

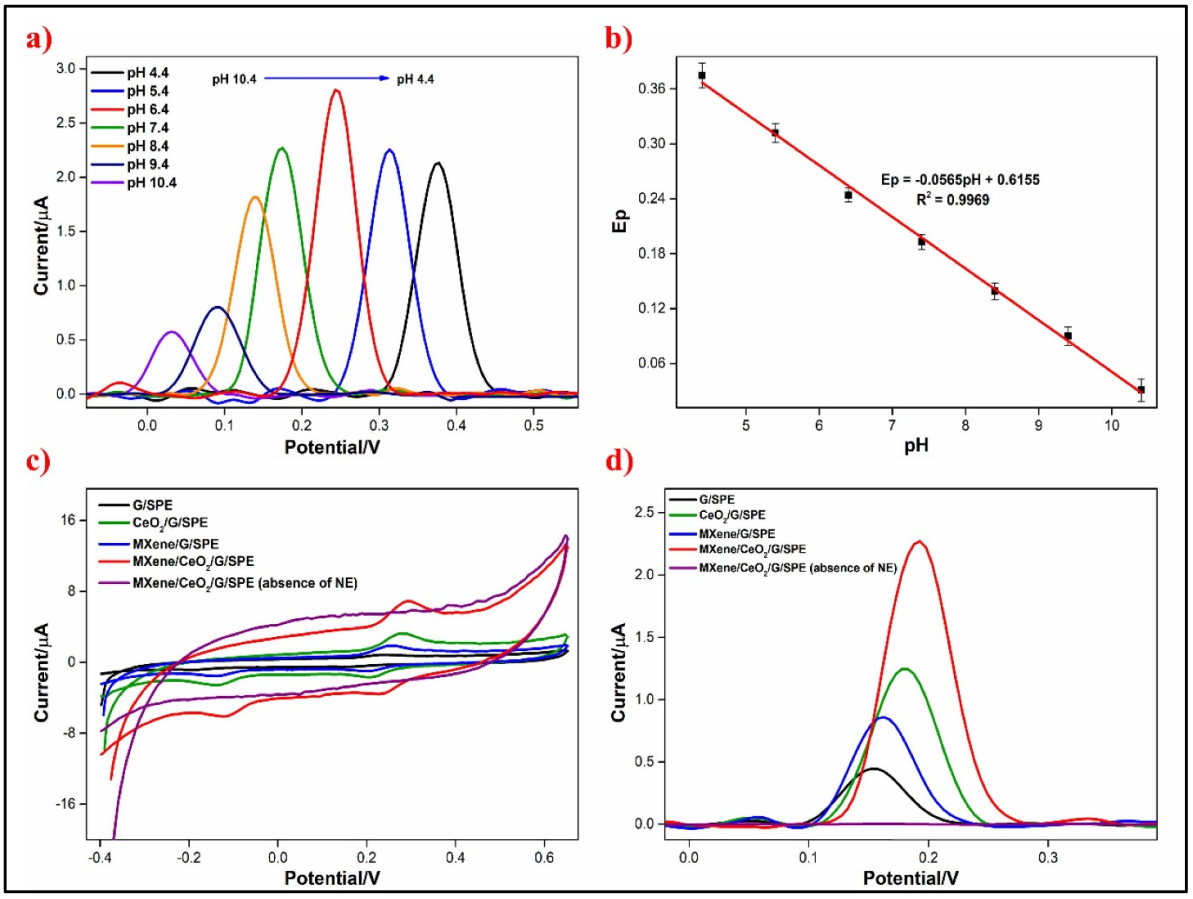


Figure 5. (a) Differential pulse voltammograms recorded at different pH values of MXene/CeO_2/G/SPE in 25 μM NE, (b) linear relationship between pH-Ep, (c) cyclic voltammograms, and (d) differential pulse voltammograms using G/SPE, CeO_2/G/SPE, MXene/G/SPE, and MXene/CeO_2/G/SPE in 0.1 M pH 6.4 PBS and 0.1 M KCl containing 25 μM NE.

Nernst Eq. 1[57]

$$Ep = E_0 - \left(\frac{2.303RT}{nF}\right) m\ pH \qquad [1]$$

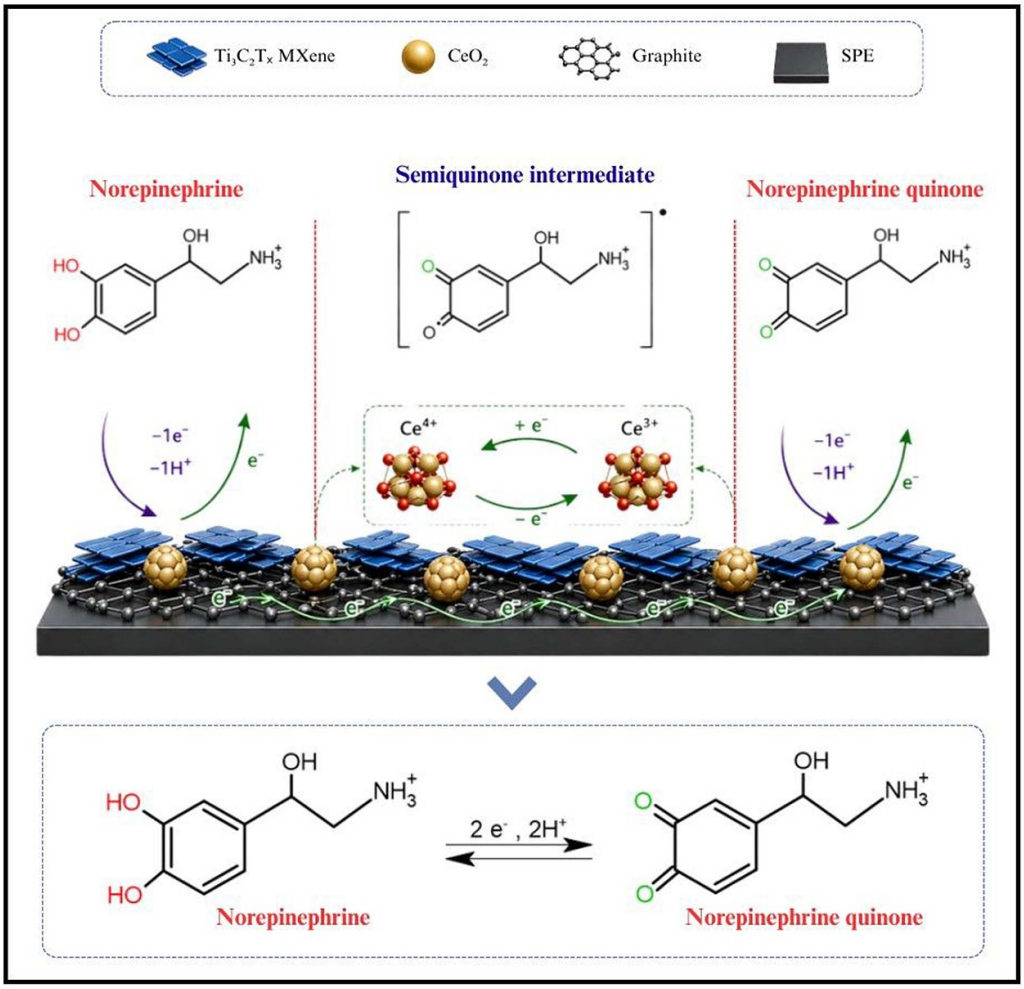
where m and n correspond to the number of protons and electrons involved in the reaction, respectively. The experimental slope (~56 mV pH^{-1}) is in close agreement with the theoretical value (59 mV pH^{-1} at 25 °C), confirming that the number of transferred protons and electrons is equal (m = n).[58]

This finding indicates a two-electron/two-proton ($2e^-/2H^+$) transfer process, which is characteristic of catecholamine oxidation.[56] Overall, these results provide strong evidence that NE oxidation at the MXene/CeO_2/G/SPE proceeds via a proton-coupled electron transfer (PCET) mechanism, offering important insight into the reaction pathway and the enhanced electrocatalytic performance of the developed sensor.

Investigation of the electrochemical behavior of NE with MXene/CeO_2/G/SPE.—The electrochemical behavior of NE was comparatively investigated via CV and DPV techniques using G/SPE, CeO_2/G/SPE, MXene/G/SPE, and MXene/CeO_2/G/SPE in a solution of 0.1 M pH 6.4 PBS and 0.1 M KCl containing 25 μM NE. As illustrated in the cyclic voltammograms (Fig. 5c), surface modification exerted a profound impact on NE oxidation. On the G/SPE, NE exhibited a negligible oxidation peak of +0.92 μA at +0.24 V, indicating sluggish electron transfer kinetics and limited electrocatalytic activity. In contrast, the incorporation of CeO_2 or MXene into the ink formulation significantly enhanced the electrochemical response, with peak currents rising to +3.34 μA and +2.03 μA, respectively. The most prominent response was achieved with the MXene/CeO_2/G hybrid SPE. This system reached an oxidation peak current of +7.04 μA at +0.29 V, representing an approximate 7.6-fold enhancement over the G/SPE. This substantial current increase is attributed to the synergistic interaction between the high metallic conductivity of MXene, which facilitates rapid electron transfer, and the redox-active Ce^{4+}/Ce^{3+} sites within the CeO_2 lattice, which increase the number of electrochemically accessible active sites and enhance the overall electrochemical response.[15,36,59] Furthermore, the high correlation between the DPV results (Fig. 5d) and CV data confirms the consistency and sensitivity of the developed sensor platform.

Scheme 2 shows the proposed electrochemical oxidation mechanism of NE at the MXene/CeO_2/G/SPE surface. During the oxidation process, the NE molecule undergoes a two-electron, two-proton transfer from its catechol group, resulting in the formation of the corresponding o-quinone structure.[56] Following this step, the oxidized species can remain in the quinone form or undergo an irreversible 1,4-intramolecular cyclization through a Michael-type nucleophilic attack of the amino group, forming a cyclized intermediate. The reduction peak observed in the voltammogram is associated with the electrochemical reduction of the oxidized NE species.[60]

Kinetic studies.—Scan rate studies were conducted to elucidate the electrochemical oxidation kinetics and mass transfer mechanism of NE on an MXene/CeO_2/G/SPE in a solution of 0.1 M pH 6.4 PBS and 0.1 M KCl containing 25 μM NE. In this context, cyclic voltammograms recorded in the range of 25–300 mV s^{-1}



Scheme 2. Electrochemical oxidation reaction mechanism of NE.

(Fig. 6a) demonstrated a direct correlation between the anodic peak currents (Ip) and the scan rate (v), accompanied by a modest positive shift in the anodic peak potentials. In Fig. 6a, the primary anodic peak observed at approximately +0.29 V was assigned to the two-electron/two-proton oxidation of NE to the corresponding open chain norepinephrine-o-quinone, while the cathodic peak at approximately +0.20 V was associated with the reduction of the remaining o-quinone back to NE. The additional low potential features can be explained by the subsequent chemical cyclization of norepinephrine-o-quinone. The initially formed o-quinone may undergo an intramolecular Michael-type addition to generate leuconoradrenochrome, which can subsequently be oxidized to noradrenochrome. Accordingly, the weak anodic peak at approximately +0.08 V and the cathodic peak at approximately −0.15 V were tentatively attributed to the leuconoradrenochrome/noradrenochrome redox couple. Similar primary and secondary redox couples have previously been reported for the electrochemical oxidation of NE.[61–63]

In order to evaluate the reaction mechanism, the variation of the peak current with respect to the scan rate (v) and the square root of the scan rate ($v^{1/2}$) was analyzed (Fig. 6b and 6d). Regression analyses revealed that the correlation coefficient obtained for the v–Ip relationship ($R^2 = 0.999$) was significantly higher than that for the $v^{1/2}$–Ip relationship ($R^2 = 0.9562$). Furthermore, the slope of the log(v)–log(Ip) plot shown in Fig. 6d was calculated to be 0.75. Since this value lies between the theoretical values of 0.5 for a diffusion-controlled process and 1.0 for an adsorption-controlled process, both diffusion from the bulk solution and adsorption at the electrode surface contribute to the oxidation of NE at the MXene/CeO_2/G/SPE surface. Accordingly, the NE oxidation process is described as proceeding through a mixed diffusion-and adsorption-controlled mechanism.[64,65] In addition, the increase in ΔEp with increasing scan rate indicates increasing kinetic polarization and is consistent with quasi-reversible electron-transfer behavior.[66] Therefore, the log(v)–log(Ip) relationship and the scan rate dependent variation in ΔEp describe distinct but complementary aspects of the overall electrochemical process: the former reflects the relative contributions of diffusion and adsorption to the peak current, whereas the latter provides information about the electron-transfer kinetics.

To further investigate the electron transfer kinetics of norepinephrine at the MXene/CeO_2/G/SPE, the scan rate dependent peak potential data were analyzed according to the Laviron equation for quasi-reversible electrochemical systems.[67] In Figs. S4a and S4b the relationships between the anodic and cathodic peak potentials and the natural logarithm of the scan rate were found to be Eqs. 2 and 3:

$$Ep_a = 0.0255\ln v + 0.3496, R^2 = 0.9936 \quad [2]$$

$$Ep_c = -0.0222\ln v + 0.1600, R^2 = 0.7468 \quad [3]$$

Based on the slopes of these plots, the number of electrons transferred, and the electron-transfer coefficient were determined using

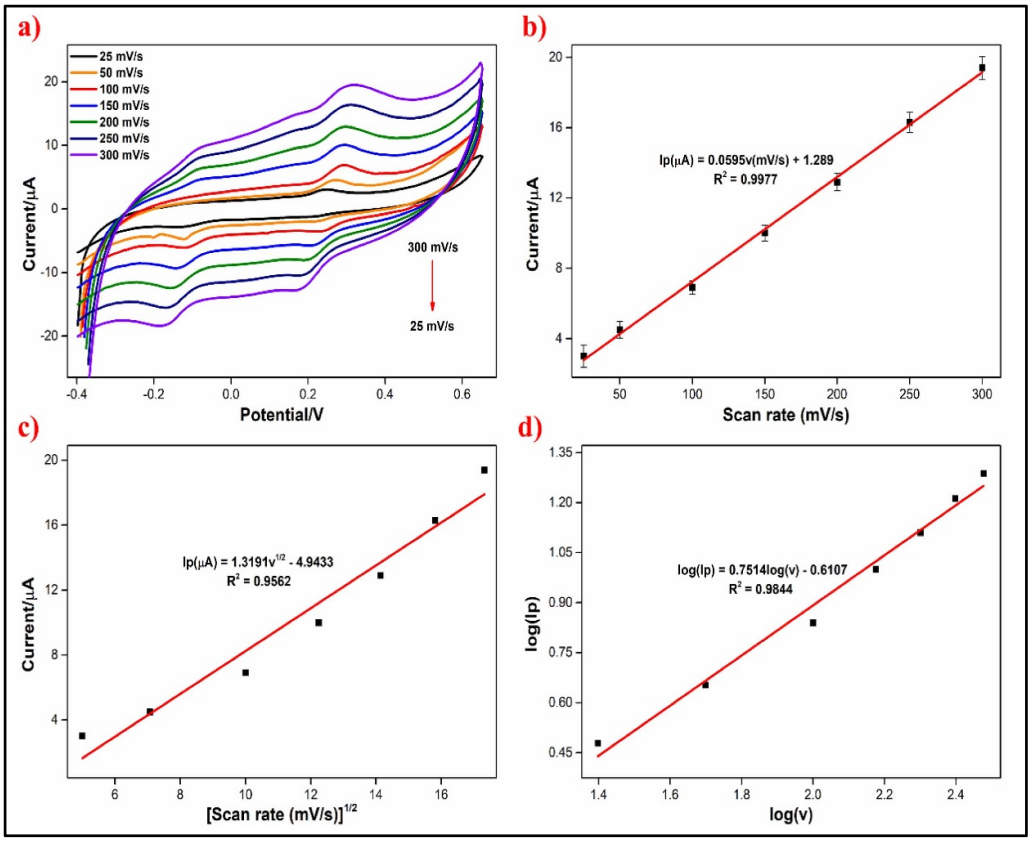


Figure 6. (a) Cyclic voltammograms obtained using MXene/CeO_2/G/SPE at different scan rates (25–350 mV s^{-1}) in a solution of 0.1 M pH 6.4 PBS and 0.1 M KCl containing 25 μM NE, (b) ν-Ip, (c) $\nu^{1/2}$-Ip, and (d) log(ν)-log(Ip) graphs.

the following Eqs. 4 and 5:

$$m_a = \frac{RT}{(1-\alpha)\,\mathrm{nF}} \quad [4]$$

$$|m_c| = \frac{\mathrm{RT}}{\alpha NF} \quad [5]$$

The calculated values of n and α were 2.16 and 0.535, respectively. The electron number, being close to the theoretical value of two, supports the two-electron redox process of NE at the MXene/CeO_2/G/SPE surface. Since the redox process exhibited quasi-reversible behavior, the apparent formal potential ($E^{0'}_{app}$) was estimated from the midpoint of the anodic and cathodic peak potentials at the lowest scan rate and was calculated to be 0.235 V. Subsequently, the apparent heterogeneous electron transfer rate constants were calculated to be 0.438 s^{-1} for the anodic process and 1.536 s^{-1} for the cathodic process. The difference between these values is attributed to the quasi-reversible nature of the electrochemical process. Overall, the Laviron analysis confirms that the proposed MXene/CeO_2/G/SPE exhibits favorable electron transfer kinetics toward NE oxidation.

In order to quantitatively evaluate the effect of electrode modification, the electroactive surface areas (A) were calculated using the Randles–Sevcik equation with a 1.0 mM $[Fe(CN)_6]^{3-/4-}$redox couple contain 0.1 M KCl.[68] The cyclic voltammograms and corresponding calibration curves for G/SPE are presented in Figs. S5a and S5b, respectively, while those for MXene/CeO_2/G/SPE are shown in Figs. S5c and S5d. The active surface area, determined to be 1.55 × 10^{-5} cm^2 for G/SPE, increased by approximately 2.5-fold to 3.98 × 10^{-5} cm^2 with the integration of MXene/CeO_2. Furthermore, the electroactive surface areas of CeO_2/G/SPE and MXene/G/SPE were also calculated in 3.63 × 10^{-5} cm^2 and 2.73 × 10^{-5} cm^2, respectively (Fig. S6). This increase is attributed to the combined effect of the high specific surface area provided by MXene and the porous structure formed by CeO_2 nanoparticles. This configuration has been demonstrated to exert a favorable influence on the interaction of NE molecules with the surface, thereby enhancing the electron transfer rate by augmenting the number of active sites on the electrode surface.

Analytical performance of MXene/CeO_2/G/SPE for NE detection.—The analytical performance of the developed MXene/CeO_2/G/SPE sensor was evaluated in terms of linear range, limit of detection (LOD), and limit of quantification (LOQ). DPV measurements were carried out at NE concentrations ranging from 0.25 to 25 μM (Fig. 7a). The results show a gradual and reproducible decrease in oxidation peak currents with decreasing NE concentration. The calibration curve (Fig. 7b), constructed from the relationship between current response and NE concentration, exhibits excellent linearity over the studied range. The corresponding calibration equation and correlation coefficient are given in Eq. 6:

$$\mathrm{Ip}\,(\mu A) = 0.1041\mathrm{C}_{[\mathrm{NE}]}\,(\mu M) + 0.1507,\ \mathrm{R}^2 = 0.9959 \quad [6]$$

Based on these results, the LOD and LOQ values were calculated to be 77.29 nM and 257.66 nM, respectively. The low LOD can be attributed to the efficient electron transfer at the modified electrode surface and the synergistic electrocatalytic effect. These results indicate that the proposed sensor provides sufficient sensitivity for the determination of NE at low concentrations.

The developed flexible MXene/CeO_2/G/SPE exhibits analytical performance comparable to or better than that of many previously

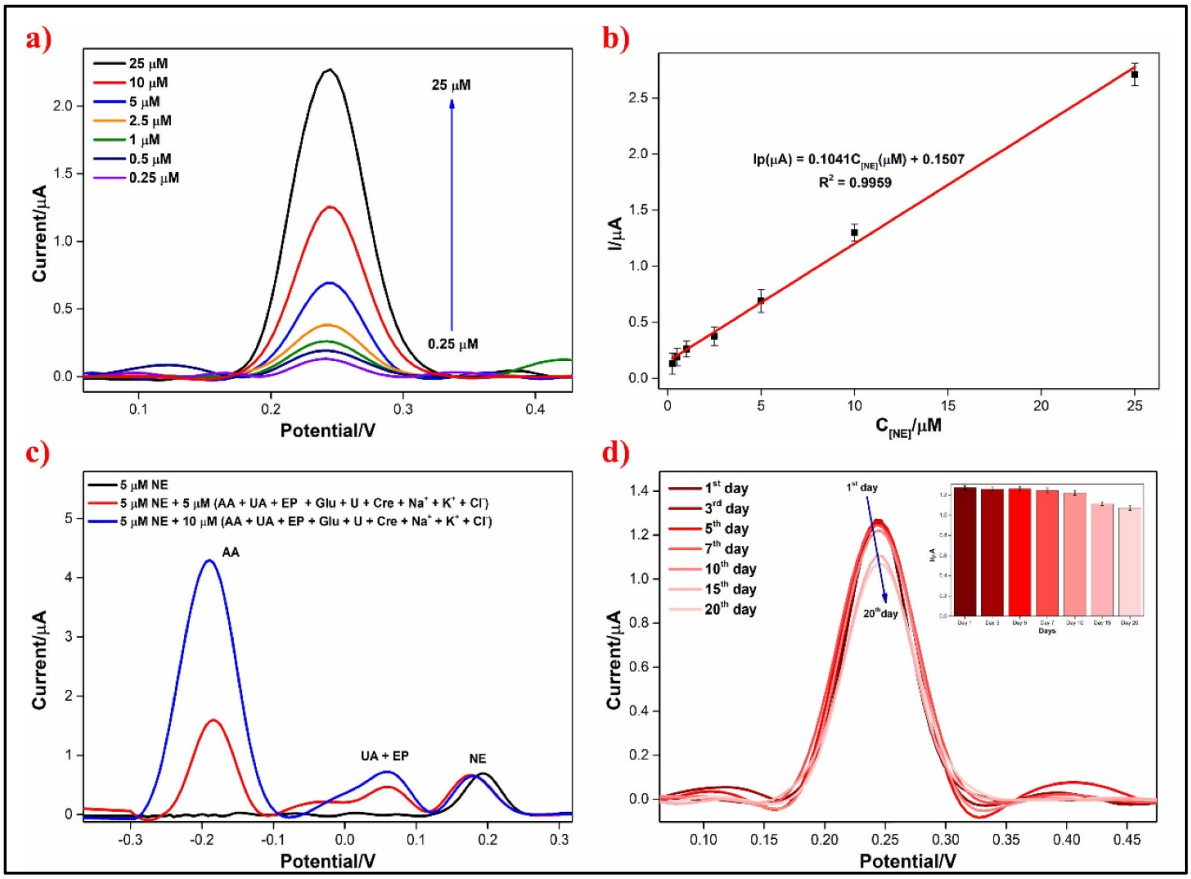


Figure 7. (a) Differential pulse voltammograms with MXene/CeO_2/G/SPE in NE solutions with different concentrations and (b) linear relationship between NE concentration and peak current, (c) differential pulse voltammograms recorded for 5 μM NE in the presence of equimolar and 10-fold excess interfering species (AA, UA, EP, Glu, U, and Cre) and (d) long-term stability of the MXene/CeO_2/G/SPE in 10 μM NE solution.

reported electrochemical sensors for NE determination (Table I). The main novelty of the proposed platform lies in the direct incorporation of MXene and CeO_2 nanoparticles into a graphite-based screen-printable conductive ink, enabling the fabricated working electrode to function simultaneously as both the conductive and electroactive sensing surface. This approach eliminates the need for additional post-printing modification steps, complex immobilization procedures, or biological recognition elements. The synergistic combination of the high electrical conductivity and large electroactive surface area of MXene with the catalytic and redox properties of CeO_2 enhances the electrochemical response toward NE. The sensor enables NE determination over a linear concentration range of 0.25–25.0 μM, with a sensitivity of 0.1041 μA μM^{-1} and a low detection limit of 77.29 nM. In addition to these favorable analytical characteristics, the sensor operates effectively under near-physiological pH conditions and provides satisfactory selectivity, reproducibility, stability, and recovery in artificial urine samples. Compared with conventional rigid and multistep-modified electrodes, the proposed platform combines flexibility, simple fabrication, disposability, and low production cost within a single screen-printed sensing system. Therefore, the MXene/CeO_2/G/SPE represents not only a sensitive platform for norepinephrine detection but also a scalable and practically applicable strategy for the fabrication of flexible electrochemical sensors.

Selectivity and reproducibility of MXene/CeO_2/G/SPE.—The analytical superiority of nanocomposite-modified SPEs, which are produced using conductive ink, is pivotal for achieving the high sensitivity and selectivity required for monitoring biological biomarkers. In this study, the selectivity of the MXene/CeO_2/G/SPE toward NE was rigorously evaluated against potential interfering species, including ascorbic acid (AA), dopamine (DA), epinephrine (EP), glucose (Glu), urea (U), creatinine (Cre), and common electrolytes (NaCl and KCl). The interfering species were selected based on previously reported electrochemical studies on norepinephrine detection.[75–77] DPV measurements were conducted in a 5.0 μM NE solution, as shown in Fig. 7c. In the absence of interferents, the NE oxidation peak current was recorded as + 0.69 μA at + 0.19 V. Upon the addition of equimolar and 10-fold higher concentrations of interfering species, the peak current remained remarkably stable at + 0.67 μA (+ 0.177 V) and + 0.66 μA (+ 0.179 V), respectively. The calculated relative errors were 2.89% and 4.35%, well within the acceptable limits for complex matrix analysis. These findings confirm that the developed sensor platform maintains high specificity for NE even in the presence of significantly higher concentrations of co-existing biological molecules.

To validate practical applicability, critical parameters such as reproducibility and long-term stability were systematically investigated. Reproducibility was assessed by performing DPV measurements with five independently fabricated MXene/CeO_2/G/SPEs under identical conditions (Fig. S7). The relative standard deviation (RSD) was calculated as 1.265%, demonstrating exceptional fabrication consistency and reliability. Furthermore, the shelf life of the MXene/CeO_2/G/SPE was monitored over 20 d in a 10 μM NE solution (Fig. 7d). The sensor exhibited robust performance with negligible signal fluctuations for the first 10 d. Although a gradual decline in the oxidation peak current was observed after day 15, with the relative error reaching 12.59% on day 20, the platform

Table I. Comparison of the analytical performance of MXene/CeO_2/G/SPE in NE determination.

Electrode	Linear range (μM)	LOD (μM)	References
NiO/MWNTs/SPCE	0.75–30.0	50.0	69
D-SWCNTs/SPCE	0.1–2.0	62.0	70
ZnO/Phthalocyanine/ MWCNT/GCE	7.5–48.0	1700	71
MIP modified-PdNPs/GCE	0.5–80.0	100.0	72
GCE/GQDs/AuNPs	0.5–0.75	150	73
ERGO-Pd/GCE	0.5–100	0.05	74
MoO_3 nanowires/GCE	0.1–2000	0.11	75
MXene/CeO_2/G/SPE	0.25–25.0	0.07729	This study

Table II. Analytical results of electrochemical norepinephrine determination in artificial urine samples using MXene/CeO_2/G/SPE.

Sample	Initial concentration (μM)	Added concentration (μM)	Found concentration (μM)	RSD (%) ($n = 3$)	Recovery (%)
Artificial urine	0.0	1.0	0.951	2.75 ± 0.026	95.10
	0.0	2.0	2.14	3.68 ± 0.076	107.00
	0.0	4.0	4.11	3.29 ± 0.133	102.75

maintained sufficient stability for short-term clinical and analytical applications.

The ∼5% signal attenuation observed after 15 d of storage is mainly attributed to the inherent susceptibility of $Ti_3C_2T_x$ MXene to oxidation. Exposure to dissolved oxygen, ambient humidity, and residual surface water can gradually convert the highly conductive MXene surface into less conductive titanium oxide (TiO_2) species. This transformation increases the interfacial charge transfer resistance and reduces the electroactive surface area.[78,79] Despite this, the relatively small signal loss indicates that the MXene/CeO_2/G largely preserves its electrochemical activity over the monitoring period, supporting its suitability for short-term sensing applications. To further minimize oxidative degradation and extend the shelf life of the MXene/CeO_2/G/SPE platform, appropriate storage conditions are essential. Storing the modified electrodes in an airtight environment at 4 °C, preferably under an inert atmosphere (e.g. nitrogen or argon) or under vacuum, can effectively slow down MXene oxidation. Since degradation is accelerated at higher temperatures and in humid environments, maintaining dry, low-temperature, and light-protected conditions is recommended to preserve both structural integrity and electrochemical performance over time.[80]

Electrochemical determination of NE in an artificial urine sample.—The practical applicability of the sensor was further evaluated by determining NE in an artificial urine sample prepared according to literature protocols.[24] Standard NE solutions at concentrations of 1, 2, and 4 μM were spiked into the artificial urine matrix, and DPV measurements were performed using the MXene/CeO_2/G/SPE. The differential pulse voltammograms (Fig. S8) show a clear and proportional increase in oxidation peak current with increasing NE concentration. To assess analytical reliability, recovery studies were carried out in the artificial urine matrix (Table II). The sensor exhibited recovery values in the range of 95.1%–107.0%, demonstrating good accuracy. Overall, these findings suggest that the MXene/CeO_2/G-based flexible sensor is a promising platform for the determination of biologically relevant molecules such as NE.

Conclusions

In this study, a flexible MXene/CeO_2/G-based conductive ink was successfully synthesized and used to fabricate disposable screen-printed electrodes on paper substrates via a simple serigraphy approach. The resulting platform was applied to the electrochemical determination of norepinephrine (NE). The sensor exhibited a wide linear range (0.25–25 μM), a low detection limit (77.29 nM), and good sensitivity, demonstrating its capability for low-level NE detection. In addition, the electrode showed satisfactory selectivity, repeatability, and applicability in artificial urine samples. The enhanced analytical performance is attributed to the synergistic effect of MXene and CeO_2, which facilitates electron transfer and increases the electroactive surface area. Overall, the proposed MXene/CeO_2/G/SPE platform offers a simple, low-cost, and scalable strategy for fabricating flexible electrochemical sensors, with promising potential for practical bioanalytical applications, particularly in point-of-care (POC) systems.

Acknowledgment

The authors would like to acknowledge that this paper is submitted in partial fulfillment of the requirements for a PhD degree at Yildiz Technical University and that the author was supported by the Scientific and Technological Research Council of Türkiye (TUBITAK) 2211-A National PhD Scholarship Program.

Author contributions

Conceptualization: Ozge Gorduk and Yucel Sahin. Experiments, data collection, and analysis: Selen Uruc, Ozge Gorduk, Semih Gorduk, and Yucel Sahin. Writing-original draft and review: All authors. All authors read and approved the final manuscript.

ORCID

Selen Uruc https://orcid.org/0000-0003-3625-8487
Ozge Gorduk https://orcid.org/0000-0003-1370-7534
Semih Gorduk https://orcid.org/0000-0001-7956-8368
Yucel Sahin https://orcid.org/0000-0001-8590-4073

References

1. R. Mostafazadeh, Y. Hamidian, N. Erk and E. N. Dragoi, *Carbon Lett.*, **33**, 1827 (2023).
2. J. A. Ribeiro, P. M. V. Fernandes, C. M. Pereira and F. Silva, *Talanta*, **160**, 653 (2016).
3. A. J. Steckl and P. Ray, *ACS Sens.*, **3**, 2025 (2018).
4. J. Park, R. V. Bhimani and C. E. Bass, *J. Electrochem. Soc.*, **165**, G3051 (2018).
5. N. Jaiswal and I. Tiwari, *J. Electroanal. Chem.*, **881**, 114956 (2021).

6. P. Pandit, B. Crewther, C. Cook, C. Punyadeera and A. K. Pandey, *Mater. Adv.*, **5**, 5339 (2024).
7. M. Zhu, X. Huang, J. Li and H. Shen, "Peroxidase-based spectrophotometric methods for the determination of ascorbic acid, norepinephrine, epinephrine, dopamine and levodopa." *Anal. Chim. Acta.*, **357**, 261 (1997).
8. N. Aoyama, M. Tsunoda and K. Imai, *J. Chromatogr. A*, **1074**, 47 (2005).
9. C. L. Guan, J. Ouyang, Q. L. Li, B. H. Liu and W. R. G. Baeyens, "Simultaneous determination of catecholamines by ion chromatography with direct conductivity detection." *Talanta*, **50**, 1197 (2000).
10. L. P. Lu, S. Q. Wang and X. Q. Lin, *Anal. Chim. Acta.*, **519**, 161 (2004).
11. E. Dokur, O. Gorduk, S. Gorduk and Y. Sahin, *J. Electrochem. Soc.*, **173**, 107504 (2026).
12. E. Dokur, O. Gorduk and Y. Sahin, *ECS J. Solid State Sci. Technol.*, **9**, 121003 (2020).
13. J. R. Camargo et al., *Microchem. J.*, **164**, 105998 (2021).
14. D. H. Ho, Y. Y. Choi, S. B. Jo, J. M. Myoung and J. H. Cho, *Adv. Mater.*, **33**, 1–29, 2005846 (2021).
15. R. Khan and S. Andreescu, *Sensors*, **20**, 1 (2020).
16. X. Huang et al., *Sci. Rep.*, **5** 1–8, 18298, (2015).
17. P. Guan, Y. Li, J. Zhang and W. Li, *Nanomaterials*, **6**, 159 (2016).
18. D. Tao, C. Xie, N. Jaffrezic-renault and Z. Guo, *Talanta*, **291**, 127863 (2025).
19. E. Sardini, M. Serpelloni and S. Tonello, *Biosensors*, **10**, 1–29, 166 (2020).
20. B. Kuswandi, M. A. Hidayat and E. Noviana, *Biosensors*, **12**, 1–22, 100246 (2022).
21. A. Ghosh, H. Pal, T. Das, S. Chatterjee and A. Das, *Mater. Today Proc.*, **58**, 714 (2022).
22. A. A. Ali, S. R. El-sayed, S. A. Shama, T. Y. Mohamed and A. S. Amin, *Desalin. Water Treat.*, **204**, 124 (2020).
23. E. Dokur, O. Gorduk and Y. Sahin, *Diam. Relat. Mater.*, **159**, 112756 (2025).
24. K. N. Parra, S. Gul, J. M. Aquino, D. W. Miwa and A. J. Motheo, *J. Solid State Electrochem.*, **20**, 1001 (2016).
25. A. Bhattarai, S. K. Shah and A. K. Yadav, "Effect of solvent composition on the critical micelle concentration of cetylpyridinium chloride in ethanol-water mixed solvent media." *Nepal J. Sci. Technol.*, **13**, 89 (2013).
26. R. Hoogenboom, H. M. L. Thijs, D. Wouters, S. Hoeppener and U. S. Schubert, *Soft Matter*, **4**, 103 (2007).
27. X. Li and K. Binnemans, *Chem. Rev.*, **121**, 4506 (2021).
28. L. Campos-arias, N. Peinka, Y. C. Lau, N. Castro, N. Pereira, V. M. G. Correia, P. Costa, J. L. Vilas-vilela and S. Lanceros-mendez, *ACS Appl. Electron. Mater.*, **6**, 2152 (2024).
29. L. M. Zhang, *Macromol. Mater. Eng.*, **286**, 267 (2001).
30. M. Rahaman, A. Aldalbahi, L. Nayak and R. Giri, *Carbon-Containing Polymer Composites* p. 159 Springer, Berlin, (2019).
31. A. Pepłowski, F. Budny, M. Jarczewska, S. Lepak-kuc, Ł. Dybowska-sarapuk, D. Baraniecki, P. Walter, E. Malinowska and M. Jakubowska, *Sensors*, **22**, 8836 (2022).
32. M. R. Somalu, V. Yufit and N. P. Brandon, *Int. J. Hydrogen Energy*, **38**, 9500 (2013).
33. M. Franco, R. Alves, N. Perinka, C. Tubio, P. Costa and S. Lanceros-mendéz, *ACS Appl. Electron. Mater.*, **2**, 2857–67 (2020).
34. M. Yang, H. Lu and S. Liu, *Appl. Sci.*, **12**, (2022).
35. C. Liang, Y. Meng, Y. Zhang, H. Zhang, W. Wang, M. Lu and G. Wang, *J. Energy Storage*, **65**, 107341 (2023).
36. K. Siposova, V. Huntosova, I. Garcarova, Y. Shlapa, I. Timashkov, A. Belous and A. Musatov, *Biomedicines*, **10**, 942 (2022).
37. H. Hao, C. Qiu, W. Qu, Y. Zhuang, X. Han, W. Tao, Y. Gu, Z. Zhao, H. Liu and W. Wang, *Chemosensors*, **12**, 128 (2024).
38. A. Fallatah and S. Padalkar, *ECS Trans.*, **80**, 1269 (2017).
39. T. H. Shin, W. Eom, K. H. Lee, W. Jeong, D. J. Kang and T. H. Han, *ACS Nano*, **15**, 3320 (2021).
40. J. Perelaer, A. W. M. De Laat, C. E. Hendriks and U. S. Schubert, *J. Mater. Chem.*, **18**, 3209 (2008).
41. S. Uruc, O. Gorduk and Y. Sahin, *J. Alloys Compd.*, **1010**, 1–15, 177786 (2025).
42. A. Chaudhary et al., *Biosensors*, **12**, 846 (2022).
43. H. Chen, Z. Zheng, H. Yu, D. Qiao, D. Feng, Z. Song and J. Zhang, *Ind. Eng. Chem. Res.*, **60**, 11128–40 (2021).
44. C. Hu et al., *Front. Chem.*, **10**, 1–7, 907777 (2022).
45. J. Chen, W. Xue, Y. Shi, J. Nan and S. Wang, *Microchem. J.*, **219**, 115950 (2025).
46. M. P. Bilibana, *Adv. Sens. Energy Mater.*, **2**, 1–27, 100080 (2023).
47. Z. Zhao et al., *Biosensors*, **15**, 246 (2025).
48. R. Siburian, H. Sihotang, S. L. Raja, M. Supeno and C. Simanjuntak, *Oriental J. Chem.*, **34**, 182 (2018).
49. I. Mansuri, R. Farzana, R. Rajarao and V. Sahajwalla, *Metals*, **8**, 290 (2018).
50. A. A. Alothman, M. R. Khan, M. D. Albaqami, S. Mohandoss, Z. A. Alothman, N. Ahmad and K. N. Alqahtani, *Nanomaterials*, **13**, 3026 (2023).
51. K. Nusrath and K. Muraleedharan, *Devagiri J. Sci.*, **2**, 118–20 (2016). (available at: www.devagirijournals.com.).
52. G. Jayakumar, A. A. Irudayaraj and A. D. Raj, *Appl. Phys. A*, **125**, (2019).
53. Y. Li, X. Zhou, J. Wang, Q. Deng, M. Li, S. Du, Y.-H. Han, J. Lee and Q. Huang, *RSC Adv.*, **7**, 24698 (2017).
54. L. Yao et al., *J. Mater. Sci.: Mater. Electron.*, **32**, 27837–48 (2021).
55. D. Channei, B. Inceesungvorn, N. Wetchakun, S. Ukritnukun, A. Nattestad, J. Chen and S. Phanichphant, *Sci. Rep.*, **4**, 5757 (2014).
56. M. A. Raj and S. A. John, *Anal. Methods*, **6**, 2181 (2014).
57. A. J. Bard and L. R. Faulkner, *Electrochemical Methods : Fundamentals and applications*, p. 833, John Wiley & Sons (2001).
58. C. Bian, Q. Zeng, H. Xiong, X. Zhang and S. Wang, *Bioelectrochemistry*, **79**, 1–5 (2010).
59. J. Zhang, K. Yu and G.-P. Wang, *Adv. Electron. Mater.*, **5** 1–10, 1900216, (2019).
60. R. Sainz et al., *Sci. Rep.*, **10**, (2020).
61. R. N. Goyal, M. A. Aziz, M. Oyama, S. Chatterjee and A. R. S. Rana, *Sens. Actuators*, **153**, 232 (2011).
62. M. D. Hawley et al., *Adrenergic Mechanisms*, p. 57, UTC, (1960). (available at: https://pubs.acs.org/sharingguidelines).
63. P. Manini, L. Panzella, A. Napolitano and M. D'ischia, *Chem. Res. Toxicol.*, **20**, 1549 (2007).
64. K. J. Aoki, J. Chen, Y. Liu and B. Jia, *J. Electroanal. Chem.*, **856**, 113609 (2020).
65. E. Laviron, *J. Electroanal. Chem.*, **52**, 395 (1974).
66. R. S. Nicholson, *Anal. Chem.*, **37**, 1351 (1965).
67. E. Laviron, *J. Electroanal. Chem. Interfacial Electrochem.*, **101**, 19 (1979).
68. E. Dokur, O. Gorduk and Y. Sahin, *FlatChem*, **51**, 100848 (2025).
69. J. Ma, Y. Xiong, Y. Wang, D. Hong and M. Zhao, *Int. J. Electrochem. Sci.*, **15**, 9325 (2020).
70. T. Rajarathinam, D. Thirumalai, M. Kwon, S. Lee, S. Jayaraman, H.-J. Paik, J. Lee and S.-C. Chang, *Bioelectrochemistry*, **146**, 1–8, 108155 (2022).
71. N. G. Mphuthi, A. S. Adekunle and E. E. Ebenso, *Sci. Rep.*, **6**, (2016).
72. J. Chen, H. Huang, Y. Zeng, H. Tang and L. Li, *Biosens. Bioelectron.*, **65**, 366 (2015).
73. A. Fajardo, D. Tapia, J. Pizarro, R. Segura and P. Jara, *J. Appl. Electrochem.*, **49**, 423 (2019).
74. S. Renjini, A. M. Pillai, P. Abraham and P. A. Pavitha, *Ionics*, **30**, 7585 (2024).
75. K. J. Samdani, D. W. Joh, M. K. Rath and K. T. Lee, *Electrochim. Acta*, **252**, 268 (2017).
76. F. M. de Morawski, B. B. Xavier, A. H. Virgili, K. D. S. Caetano, E. W. de Menezes, E. V. Benvenutti, T. M. H. Costa and L. T. Arenas, *Mater. Sci. Eng. C*, **120**, 1–12, 111646 (2021).
77. S. Boobphahom et al., *Microchim. Acta*, **188**, 387 (2021).
78. Q. Wang, N. Han, Z. Shen, X. Li, Z. Chen, Y. Cao, W. Si, F. Wang, B.-J. Ni and V. K. Thakur, *Nano Mater. Sci.*, **5**, 39–52 (2023).
79. T. Habib, X. Zhao, S. A. Shah, Y. Chen, W. Sun, H. An, J. L. Lutkenhaus, M. Radovic and M. J. Green, *NPJ 2D Mater. Appl.*, **3**, (2019).
80. S. Uruc, O. Gorduk, S. Gorduk and Y. Sahin, *Diam. Relat. Mater.*, **165**, 113628 (2026).